Nanoscale Advances

PAPER

View Article Online
View Journal | View Issue

Check for updates

Cite this: *Nanoscale Adv.*, 2020, **2**, 3323

Mechanistic insight into biopolymer induced iron oxide mineralization through quantification of molecular bonding†

K. K. Sand, ‡§*[ab] S. Jelavić, §[c] S. Dobberschütz,[c] P. D. Ashby,[b] M. J. Marshall,[d] K. Dideriksen, ¶[c] S. L. S. Stipp,‖[c] S. N. Kerisit,[a] R. W. Friddle[e] and J. J. DeYoreo*[af]

Microbial production of iron (oxyhydr)oxides on polysaccharide rich biopolymers occurs on such a vast scale that it impacts the global iron cycle and has been responsible for major biogeochemical events. Yet the physiochemical controls these biopolymers exert on iron (oxyhydr)oxide formation are poorly understood. Here we used dynamic force spectroscopy to directly probe binding between complex, model and natural microbial polysaccharides and common iron (oxyhydr)oxides. Applying nucleation theory to our results demonstrates that if there is a strong attractive interaction between biopolymers and iron (oxyhydr)oxides, the biopolymers decrease the nucleation barriers, thus promoting mineral nucleation. These results are also supported by nucleation studies and density functional theory. Spectroscopic and thermogravimetric data provide insight into the subsequent growth dynamics and show that the degree and strength of water association with the polymers can explain the influence on iron (oxyhydr)oxide transformation rates. Combined, our results provide a mechanistic basis for understanding how polymer–mineral–water interactions alter iron (oxyhydr)oxides nucleation and growth dynamics and pave the way for an improved understanding of the consequences of polymer induced mineralization in natural systems.

Received 19th February 2020
Accepted 12th June 2020

DOI: 10.1039/d0na00138d

rsc.li/nanoscale-advances

Open Access Article. Published on 15 June 2020. Downloaded on 4/30/2026 12:16:13 PM.
This article is licensed under a Creative Commons Attribution-NonCommercial 3.0 Unported Licence.

Introduction

Microbially produced iron (oxy)hydroxides have a large impact on the global iron cycle[1] and have influenced the creation of an oxygen-rich atmosphere.[2] For common iron oxidizers such as *Gallionella* (Fig. 1a) and iron reducers such as *Shewanella* (Fig. 1b) we find nanoparticles of hydrated iron phases on their filamentous polysaccharide rich stalks[3] and extracellular polymeric substances (EPS) respectively.[4,5] This intimacy suggests that the organic compounds are involved in the nucleation process of the iron phases. The microbial polymers are known to strongly affect subsequent nanoparticle behaviour in soils and sediments such as growth,[6–9] transformation,[10,11] aggregation[9,11,12] and reactivity.[3,11,13,14] Yet, we do not know if the polymers drive the nucleation or if they merely adsorb at the already formed nanoparticles. In the case of directed control of polymers over nanoparticle nucleation, the formation of nanoparticles can occur at a lower driving force (*e.g.* supersaturation) than currently assumed, which will add to the significance of microbial biomineralization in the iron and carbon cycles. Currently, the physicochemical controls exerted by these biopolymers on iron (oxyhydr)oxide behaviour is poorly understood which makes it difficult to assess the impact of such interactions on an environmental level.

Iron (oxyhydr)oxides are common products of aqueous processes and are readily found in soils and sediments.[15] In solution, iron (oxyhydr)oxides form by attachment of primary entities such as ionic complexes[16] or poorly to well crystalline nanoparticles.[6,17–20] The size of the primary entities is between ~1–4 nm.[6,16] In oxic environments, ferrihydrite ($\sim Fe_{8.2}O_{8.5}(OH)_{7.4}\cdot 3H_2O$), an iron (oxyhydr)oxide with the smallest particle size among iron oxides, is one of the most stable phases at the nanoscale[21] and is generally the first one to precipitate. It is poorly crystalline, has highly charged surface sites and transforms to other iron (oxyhydr)oxides over time.[22] At

[a]*Physical Sciences Division, Pacific Northwest National Laboratory, Richland, WA, USA. E-mail: kas84@aber.ac.uk; james.DeYoreo@pnnl.gov*

[b]*Molecular Foundry, Lawrence Berkeley National Laboratory, Berkeley, CA, USA*

[c]*Nano-Science Center, Department of Chemistry, University of Copenhagen, Denmark*

[d]*Biologic Sciences Division, Pacific Northwest National Laboratory, Richland, WA, USA*

[e]*Sandia National Laboratories, Livermore, California 94550, USA*

[f]*Department of Material Science and Engineering, University of Washington, Seattle, WA, USA*

† Electronic supplementary information (ESI) available. See DOI: 10.1039/d0na00138d

‡ Current address: Geography & Earth Sciences, Aberystwyth University, UK.

§ Current address: Section for GeoGenetics, Globe Institute, Faculty of Health and Medical Sciences, University of Copenhagen, Denmark.

¶ Current address: Department of Geochemistry, Geological Survey of Denmark and Greenland (GEUS), Denmark.

‖ Current address: Department of Physics, Technical University of Denmark, Denmark.

Open Access Article. Published on 15 June 2020. Downloaded on 4/30/2026 12:16:13 PM.
This article is licensed under a Creative Commons Attribution-NonCommercial 3.0 Unported Licence.

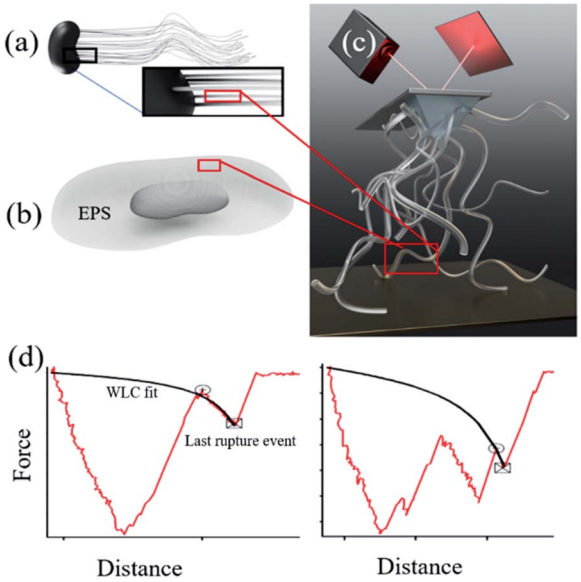

Fig. 1 (a) Polysaccharide stalks from *Gallionella* and (b) EPS produced by *Shewanella* are both associated with iron (oxyhydr)oxide formation. (c) We covalently attached alginate and EPS to an AFM tip and brought the polymers in contact with ferrihydrite and hematite and obtained dynamic force spectra. (d) Force curves typycal for interaction between polymer brushes and minerals. Distance along the *y*-axis is the length between the surface and the tip pulling away from the surface. To derive single polymer binding events, we applied worm-like chain fits (black curve) for the last rupture event for each force curve.

circumneutral pH, a common product of ferrihydrite transformation is hematite (Fe_2O_3), which is the most stable macroscopic iron oxide.[21,23] Hematite has a low surface charge and well developed crystal faces, where the most stable crystal face is the {00.1}.[24,25] The formation of ferrihydrite in solution[26,27] and its subsequent transformation[28,29] has long been investigated but the mechanisms underlying the nucleation of iron (oxyhydro)oxides and their transformation behaviour on substrates, such as biopolymers, is lacking.

Considering the principles of nucleation theory, there are two main processes by which polymers can facilitate nucleation: by locally increasing the ion activity and the supersaturation[30] or by decreasing the free interfacial energy of the polymer–nuclei–solution system, γ.[31,32] One hypothesis is that microbial polymers decrease γ for iron (oxyhydr)oxide formation, thus reducing the system's free energy barrier to nucleation, ΔG^*, which is proportional to γ^3 through:[33]

$$\Delta G^* = \frac{F\omega^2\gamma^3}{k_B T\sigma^2}, \quad (1)$$

where ω represents the molecular volume, k_B, the Boltzmann constant, T, the temperature and σ, the saturation. Because nucleation probability scales exponentially with ΔG^*, a small decrease in γ of the polymer–nuclei-solution has a huge impact. This was previously demonstrated for nucleation of a relatively soluble mineral, calcite ($CaCO_3$), on polysaccharides[33] and a direct method to test this hypothesis was established in a separate study,[34] which confirmed the theoretical prediction[35] that, for any heterogeneous nucleation process, γ of polymer–nuclei-solution system is directly proportional to the free energy of crystal-substrate binding (*i.e.*, adhesion), ΔG_{adh}:

$$\gamma = -\frac{h}{a}\Delta G_{adh} + (1+h)\gamma_{CL}, \quad (2)$$

where h represents a nucleus shape factor, a, the area of interaction per molecule and γ_{CL}, the crystal–liquid interfacial free energy. This means that large ΔG_{adh}, independent of any additional effects from a substrate (*e.g.* enhanced ion binding[30]), would translate into a reduced γ and hence a decreased ΔG^*. Here, we use this relationship established for polymer–calcite system to investigate whether polymer–iron (oxyhydr)oxide binding is strong enough to decrease the interfacial free energy for formation of poorly soluble iron (oxyhydr) oxides and hence, to determine whether this is the driving mechanism behind their formation on biopolymers.

It has been difficult to experimentally determine ΔG_{adh} at the bond level between minerals and polymer assemblies (polymer brush) such as polysaccharide and EPS. DFS is an atomic force microscopy (AFM) based technique that have been used to address binding between a polymer and a substrate. DFS measures the force required to rupture the bond, f_r, between a substrate and a polymer attached to the AFM tip (Fig. 1c), as a function of loading rate, l_r. This approach has traditionally been challenging to apply for a polymer brush because of both analytical challenges related to interpret the non-linear dependence of extension as well as unravelling the unknown amount of bonds clustered at the probe–surface contact. The latter has been circumvented by having just one (or a few) molecules on the tip. However, a polymer brush is a better representation of a natural system and would allow us to take intramolecular forces between the biopolymers into account. Recently, however, a new approach was formulated where direct information about the interaction between extendable polymer brushes and mineral surfaces was obtained.[36] The approach is polymer brush-based dynamic force spectroscopy (DFS).[36] The polymer brush-based approach provides a way for extracting rupture forces that approximate single polymer events from a polymer coated probe. This technique is highly relevant for natural systems when polymers often occur in close proximity and polymer–polymer interactions take part in the overall binding. We used alginate polysaccharide as a model for polysaccharide rich bacterial stalks and EPS extracted from *Shewanella* as a real representation of the extracellular environment where bacteria influence iron (oxyhydr)oxide precipitation. Besides polysaccharides, EPS can contain proteins, nucleic acids, phospholipids and humic substances[37] but polysaccharides have been shown to play a decisive role in iron (oxyhydr)oxide crystallisation and geochemical cycling.[3,38,39] We covalently attached alginate and EPS to AFM tips and collected force curves from surfaces of either ferrihydrite nanoparticles or a polished, single crystal of hematite {00.1} (Fig. S1†). The large hematite crystal ensures that we are probing only this most stable and most represented face. The nanoparticulate ferrihydrite substrate ensures that we are probing a variety of possible

 This journal is © The Royal Society of Chemistry 2020

Open Access Article. Published on 15 June 2020. Downloaded on 4/30/2026 12:16:13 PM.
This article is licensed under a Creative Commons Attribution-NonCommercial 3.0 Unported Licence.

surfaces characteristic for such a poorly crystalline and yet structurally unresolved iron (oxyhydr)oxides.

If indeed the polymers decrease γ, we would expect the polymer–nuclei-solution system to form smaller nuclei compared to a polymer-free system because a lower nucleation barrier would result in more nuclei compared to a system with a higher barrier. Thus, we tested the results from the binding experiments performed on ferrihydrite and hematite surfaces to bulk nucleation experiments. For the bulk experiments, we coprecipitated alginate-containing and alginate-free ferrihydrite and used pair distribution function (PDF) and transmission electron microscopy (TEM) to determine the resulting particle size. In addition, we used cryogenic X-ray photoelectron spectroscopy (XPS) and thermogravimetric analysis (TGA) to gain information on the transformation processes. Additionally, we used density functional theory (DFT) to support the findings. Our results are consistent across scales, from single-molecule binding experiments and simulations to bulk nucleation studies.

Experimental

Preparation of hematite and ferrihydrite substrates for DFS

We used the {00.1} face from a polished, single crystal of hematite as a substrate for DFS measurements. The {00.1} face was cleaned in 1 M NaOH at 60 °C for 1 h to remove fatty contamination, sonicated for 20 min to remove particulate contaminants, rinsed with ultradeionised water (MilliQ, resistivity 18.2 MΩ cm) and plasma cleaned for 10 min prior to use. This cleaning procedure results with hematite adventitious carbon content of 6.9 ± 0.7 at%.[40] The hematite substrate was imaged using *Cypher ES™ Environmental* to confirm the flatness of the surface and the absence of a particulate contamination ((ESI), Fig. S1†).

For preparation of ferrihydrite substrate, we used reagent grade NaOH (Sigma Aldrich, ≥98%) and $Fe(NO_3)_3 \cdot 9H_2O$ (Sigma Aldrich, ≥98%). The ferrihydrite substrate was made by nucleating iron (oxyhydr)oxide on freshly cleaved muscovite (Ted Pella Inc., mica grade V-3) using the protocol of Jun *et al.*[41] After 20 minutes, we obtained a substrate of closely packed ferrihydrite particles. The adventitious carbon content of such prepared ferrihydrite substrate, measured with XPS, was 8.3 ± 0.4 at%. Prior to DFS experiments, a ferrihydrite substrate was imaged in air or liquid using a *Cypher ES™ Environmental* or a *MFP3D* AFM to confirm uniform coverage (Fig. S1†).

Tip functionalization

We functionalised the tips with (a) alginate (Pronova UP LVM, Novamatrix, Norway) and (b) a saccharide-rich and protein-poor (ratio 3.64 : 1) EPS fraction extracted from the biofilm of *Shewanella oneidensis* strain MR-1, using the procedure from Cao *et al.*[42] To functionalize the tips, the alginate and EPS were covalently attached to sharpened silicon nitride MSCT tips from *Bruker* (nominal spring constant, k = 0.01–0.6) using the protocol from Sletmoen *et al.*[43] Briefly, the AFM tips were thoroughly rinsed using 3 sequences of ethanol and MilliQ water and after drying, they were plasma cleaned for 10 minutes, then silanized in freshly prepared 1% (v/v) solution of trimethoxysilylpropyl–diethylenetriamine and 1 mM acetic acid, for 20 min at room temperature, then rinsed in MilliQ water. 1-(3-Dimethylaminopropyl)-3-ethylcarbodiimide hydrochloride (EDAC) was used as a coupling agent between the amino groups of the silanized AFM tips and the carboxylate on the polysaccharide. 0.5 mg ml^{-1} EDAC was incubated for 1 h with 20 μg ml^{-1} alginate or EPS in 50 mM boric acid, pH 5.8.

DFS data acquisition

DFS is a method to directly measure the forces between a complex organic molecules and a mineral surface. These forces are then recalculated into bond parameters used to derive thermodynamic parameters such as ΔG_{adh}. DFS measurements were made using an *Asylum MFP3D* AFM at 20 °C in 10 mM NaCl (Sigma Aldrich, ≥99.5%). 10 mM NaCl solution was used to minimise the repulsive van der Waals forces between the tip and substrate and to avoid possible complexation between PS/EPS and divalent cations. All solutions were filtered through a 0.22 μm filter (Whatman) prior to use. To avoid damage to the tip during the force measurements, we used the minimum trigger force possible (in general, 120 pN) and determined the true cantilever spring constant at the end of the measurement. The spring constant was measured using the thermal calibration method,[44] at a trigger point of 2500 pN. Subsequently, the tip was discarded. During the DFS measurements, we used a constant approach rate of 500 nm s^{-1} and a dwell time of 1 s. We collected force curves for seven retraction velocities, for each experiment, ranging from 5 nm s^{-1} to 10 μm s^{-1}, to sample energy profiles in both the near equilibrium and far from equilibrium regimes. The retraction velocity was changed every 5 force curves, while the tip probed random points on the surface. This approach minimized the effect of local mineral heterogeneities. A minimum of 20 such cycles was made for each experiment, resulting in at least 700 force curves per experiment.

DFS data analysis

We used the single bond theory developed by Friddle *et al.*[45] for data interpretation, where f_r is plotted against the l_r. We used the polymer brush-based approach developed by Sand *et al.*[36] for the data treatment. In brief, to approximate single polymer event, we only considered the rupture events that most likely represent the rupture/bond breaking between a single polymer and the substrate. Because of tip geometry, the last rupture event, *i.e.* the event where the tip is furthest from the substrate, has the highest likelihood of representing a single rupture event. To further discriminate between multiple and single rupture events, we applied the worm-like chain (WLC) model to that last rupture event to estimate the number of interacting molecules, N, involved in the rupture:

$$\frac{fL_{app}}{k_B T} = \frac{x}{L} + \frac{1}{4\left(1 - \frac{x}{L}\right)^2} - \frac{1}{4} \quad (3)$$

Open Access Article. Published on 15 June 2020. Downloaded on 4/30/2026 12:16:13 PM.
This article is licensed under a Creative Commons Attribution-NonCommercial 3.0 Unported Licence.

and

$$L_{app} = \frac{L_p}{N}, \quad (4)$$

where f represents the force, L_{app} represents the apparent persistence length, L, the contour length of the polysaccharide, x, the tip-surface separation and L_p, the persistence length of a single polymer. L_{app} describes the steepness of each force curve. L_{app} decreases with increasing number of polymer molecules participating in the adhesion cluster. Thus, measurements with the highest recurring persistence length most closely correspond to a single polymer and therefore approximate a single polymer rupture event.[36] All curves were fit with the WLC model. We discarded the curves with poor fit parameters (a WLC fitting parameter, R, lower than 80%, and an error above 10% of the L_{app} value (the standard deviation of the $L_{app} \times 100/L_{app}$)). Of those statistically selected curves, we only accepted the force curves with $L_{app} > 1$ nm in order to approximate single polymer interactions (histogram (Fig. S10), more information in the ESI-Section 11†). That gave a final set of curves with an average R of 93% ± 3 for the WLC fit and showed that 90, 94 and 87 curves approximate a single polymer event for alginate–hematite, alginate–ferrihydrite and EPS–ferrihydrite, respectively. This number of single polymer events is considerably larger than the 6 force curves needed to describe a single bond interaction, at a 99% confidence level.[46] Following the approach of Sand *et al.*,[36] rupture events were filtered for curves showing the highest persistence lengths. For those measurements, we calculated the actual/true loading rate by measuring the change in force over time, $l_r = dF/dT$. The filtered curves were plotted as the mean rupture force *vs.* mean loading rate. An example of the histograms of rupture forces and loading rate distributions for one data point in the equilibrium regime for each experimental set is included in Fig. S11.† We determined experimental values for the equilibrium force, f_{eq}, distance between transition states, x_t, and intrinsic unbinding rate, k_{off}, by fitting our rupture forces for the single polymer events *vs.* loading rate to the equation:[45]

$$\langle f \rangle \cong f_{eq} + f_\beta e^{\frac{1}{R(f_{eq})}} E_1\left(\frac{1}{R(f_{eq})}\right), \quad (5)$$

where

$$R(f_{eq}) = \frac{l_r}{k_u(f_{eq})f_\beta}, \quad (6)$$

$$E_1(z) = \int_z^\infty \frac{e^{-s}}{s} ds, \quad (7)$$

and where $f_\beta = k_B T/x_t$.

We calculated the adhesion free energy per unit length following the polymer brush-based approach.[36] Manohar *et al.*,[47] related f_{eq} to the adhesion free energy per unit length, γ_{adh}, by:

$$\gamma_{adh} = \frac{k_B T}{b} \ln\left(\frac{4\pi \sinh\left(\frac{f_{eq} b}{k_B T}\right)}{\frac{f_{eq} b}{k_B T}}\right), \quad (8)$$

where b represents the Kuhn length of the polymer ($b = 2L_p$). For large values of the argument, $f_{eq} b/k_B T \gg 1$, Manohar *et al.*[48] has shown that eqn (8) reduces to (ESI Section 13†):

$$\gamma_{adh} \approx f_{eq}. \quad (9)$$

The free energy of adhesion per monomer then follows as:

$$\Delta G_{adh} = \gamma_{adh} l_{mono} \approx f_{eq} l_{mono}, \quad (10)$$

where the monomer length $l_{mono} = 0.675$ nm represents the sum of a saccharide ring length (0.483 nm)[49] with the length of the carboxyl group expected to be involved in the bonding (0.192 nm).

Density functional theory (DFT)

Plane-wave DFT calculations were performed with the projector augmented-wave (PAW)[50,51] method, as implemented in the *ab initio* total energy and molecular dynamics program VASP (Vienna *Ab initio* Simulation Package).[52–54] The calculations made use of the Perdew–Burke–Ernzerhof (PBE)[55,56] generalized gradient approximation (GGA) of the exchange-correlation potential. The rotationally-invariant variant to the DFT+U approach[57] was employed to treat the Fe 3d electrons with an effective on-site parameter U_{eff} of 3.81 eV,[58] on the surface of interest to this work. A plane-wave cutoff energy of 600 eV was used throughout. A 2 × 2 hydroxyl-terminated {00.1} hematite slab with 4 iron bilayers was constructed from the crystallographic structure of Blake *et al.*[59] An alginate monomer was initially placed with its center of mass approximately 5 Å above the surface. A constant volume *ab initio* molecular dynamics (AIMD) simulation was then run at 50 K for 5 ps to let the alginate monomer bind to the surface. The AIMD simulation was followed by energy minimization with the conjugate gradient approach. Energy minimizations of the isolated hematite surface and alginate monomer were performed to calculate the alginate adsorption energy at the {00.1} surface. An energy minimization with 3 water monolayers was also made to compare the alginate adsorption energy to that of water.

Synthesis of hematite and ferrihydrite nanoparticles, and their coprecipitates and complexes with alginate

Hematite was precipitated following the protocol of Barton *et al.*,[60] by slowly dripping 60 ml of 2 M iron(III) nitrate ($Fe(NO_3)_3 \cdot 9H_2O$) (Sigma Aldrich, ≥98%) solution into 750 ml of boiling MilliQ. The reaction time was approximately 30 min, after which the solution was removed from the heater and left overnight, at a room temperature, to cool. The next day, the solution was poured into MilliQ water rinsed dialysis bags (Spectra/Por tubing) and dialyzed against MilliQ water until the conductivity of solution approached that of MilliQ water (7 days).

Ferrihydrite was prepared following the method of Schwertmann and Cornell.[23] We added 1 g $Fe(NO_3)_3 \cdot 9H_2O$ (Sigma Aldrich, ≥98%) to 12.5 ml MilliQ water and dropwise added 1 M NaOH at 2 ml min^{-1} under vigorous stirring. When

 This journal is © The Royal Society of Chemistry 2020

Open Access Article. Published on 15 June 2020. Downloaded on 4/30/2026 12:16:13 PM.
This article is licensed under a Creative Commons Attribution-NonCommercial 3.0 Unported Licence.

pH reached 6.8, the titration was stopped and the precipitates centrifuged and rinsed 3 times in MilliQ water.

When ferrihydrite was coprecipitated with alginate polysaccharide (Pronova UP LVM, Novamatrix, Norway), alginate was added to MilliQ water to obtain a total concentration of 0.1% PS. The PS-MilliQ solution was adjusted with 1 M HCl to pH 2.5 before starting the titration, which was made in the same way as for the pure ferrihydrite precipitate. Once the titration stopped, the suspension was centrifuged and rinsed 3 times in MilliQ water.

Hematite could not have been coprecipitated with alginate because the water-boiling temperature during the synthesis would degrade the alginate. To make TGA and cryoXPS analyses comparable for ferrihydrite and hematite, we prepared mixtures of ferrihydrite with alginate, and hematite with alginate. We added ferrihydrite and hematite powders to 10 mM NaCl, 0.1% (w/w) alginate solution and kept the specific surface area/liquid ratio the same. The 15 ml PET tubes containing alginate–iron (oxy/hydr)oxide complexes were shaken overnight, ultracentrifuged and washed by ultracentrifugation with 45 ml of 10 mM NaCl solution to remove excess alginate, then freeze-dried.

Characterisation of (alginate-) ferrihydrite and (alginate-) and hematite nanoparticles

X-ray diffraction (XRD). The diffractograms were recorded in reflection mode on a *Bruker D8 Advance*, using Cu K_α radiation (λ = 1.54 Å) and a LynxEye silicon strip PS detector. Samples were mounted on Si low-background sample holders and the scattering from the powders was recorded from 10–90° 2Θ with step size of 0.04° 2Θ and 3 s counting time. The sample was spun at 20 rpm. We used 0.3° primary and 3° secondary slits, 2.5° Soller slits on incident and diffracted beams and a 0.02 mm thick Ni filter. The diffractograms of pure hematite and ferrihydrite are shown in ESI (Fig.S2†).

Pair distribution function (PDF). X-ray scattering data for pair distribution function (PDF) analyzes were obtained at beam line 11-ID-B at the Advanced Photon Source, Argonne National Laboratory. The X-ray energy was 58.66 keV and scattered X-rays were detected with a 40 cm × 40 cm amorphous Si 2D detector (Perkin Elmer), placed approximately 15 cm from the sample. From measurement of a CeO_2 standard, the geometry of the experimental setup was calibrated using the software Fit2D.[61] Samples were mounted in Kapton capillary tubes (Cole-Parmer) and measured for 5 min. The obtained 2D data were converted to polarization corrected 1D data with Fit2D. PDFs were then obtained with the software PDFGETX2,[62,63] using standard data treatment procedures, including subtraction of the background measured for an empty sample holder, subtraction of the incoherent scattering, normalization by the average atomic scattering cross section, correction for nonlinear detector efficiency and Fourier transform of the reduced scattering structure function ($Q[S(Q) - 1]$). For data treatment, the composition of ferrihydrite was assumed to be $Fe_{8.2}O_{8.5}(OH)_{7.4}\cdot 3H_2O$, based on the composition for the 2 nm varian.[64] A maximum Q of 24 $Å^{-1}$ was used for the Fourier transform of $Q[S(Q) - 1]$. The software PDFgui[65] was used to calculate PDFs based on the structure for 2 nm ferrihydrite[66] and the structural parameters and the size of the coherent scattering domains were fitted to minimize difference between calculated and measured patterns. All parameters were fitted in the order: (1) scale, correlated atomic movement (δ_2), spherical size of coherent scattering domains, (2) unit cell dimension, (3) isotropic atomic displacement parameters, (4) Fe occupancy and (5) atomic position constrained within the space group of the ferrihydrite model ($P6_3mc$). Prior to the ferrihydrite fitting, instrument dampening (Q_{damp}) of 0.047 was determined from fit to the measured PDF for synthetic, well crystallized goethite.

Transmission electron microscopy (TEM). Droplets of the suspended ferrihydrite and ferrihydrite–alginate particles were deposited on TEM grids, dried and imaged with a field emission *JEM2100-F* (JEOL Ltd) operated at 200 kV.

Thermogravimetric analyses (TGA). Around 40 mg of solid was added to the crucible and data were obtained from 30 to 1000 °C with a heating rate of 10 °C min^{-1} under N_2 atmosphere using a *Netzsch TG 209 Libra*.

X-ray photoelectron spectroscopy (XPS). We used XPS at room temperature and in cryogenic mode (cryoXPS) for *in situ* investigation of the composition of the solid–solution interface.[67–69] The instrument was a *Kratos Axis Ultra^{DLD}* spectrometer operated with Al monochromatic K_α radiation (1486.6 eV; 150 W). A charge neutraliser was used to compensate for the charging resulting from the photoelectron emission. We used CasaXPS to fit the data and the Shirley algorithm for background subtraction. The binding energy (BE) scale was calibrated by setting the O 1s energy to 530.0 eV.[70] The photoelectron peaks were fitted using a combination of 30% Gaussian and 70% Lorentzian contributions. We prepared suspensions of ferrihydrite and hematite nanoparticles in 0.1% alginate solution and in pure MilliQ and adjusted pH to 5.5 ± 0.1. The suspensions were left to equilibrate for 18 hours in 15 ml PET tubes. The data acquisition protocol was previously described by Jelavić *et al.*[71] In short, the suspensions were ultracentrifuged for 10 min and the supernatant was decanted, a small amount of the wet sediment was transferred directly to the XPS antechamber precooled with liquid nitrogen to ~170 °C where the wet paste immediately vitrified. The sample was then transferred to the analysis chamber also cooled at ~170 °C with liquid nitrogen and analysed, under ultrahigh vacuum conditions, ~10^{-9} Torr (V-vitrified sample). Once the analysis in cryogenic conditions was done, the liquid nitrogen line was disconnected and the sample was then left in the analysis chamber overnight to warm up to ambient temperature. The next morning, the same sample was analysed at ambient temperature and the similar vacuum conditions (RT-room temperature sample). As a reference, we recorded dry powders of ferrihydrite, hematite and alginate at ambient temperature (Fig. S3†).

Results and discussion

For all force curves, we observed the characteristic saw tooth pattern for polymer detachment (red curves in Fig. 1d) that

Open Access Article. Published on 15 June 2020. Downloaded on 4/30/2026 12:16:13 PM.
This article is licensed under a Creative Commons Attribution-NonCommercial 3.0 Unported Licence.

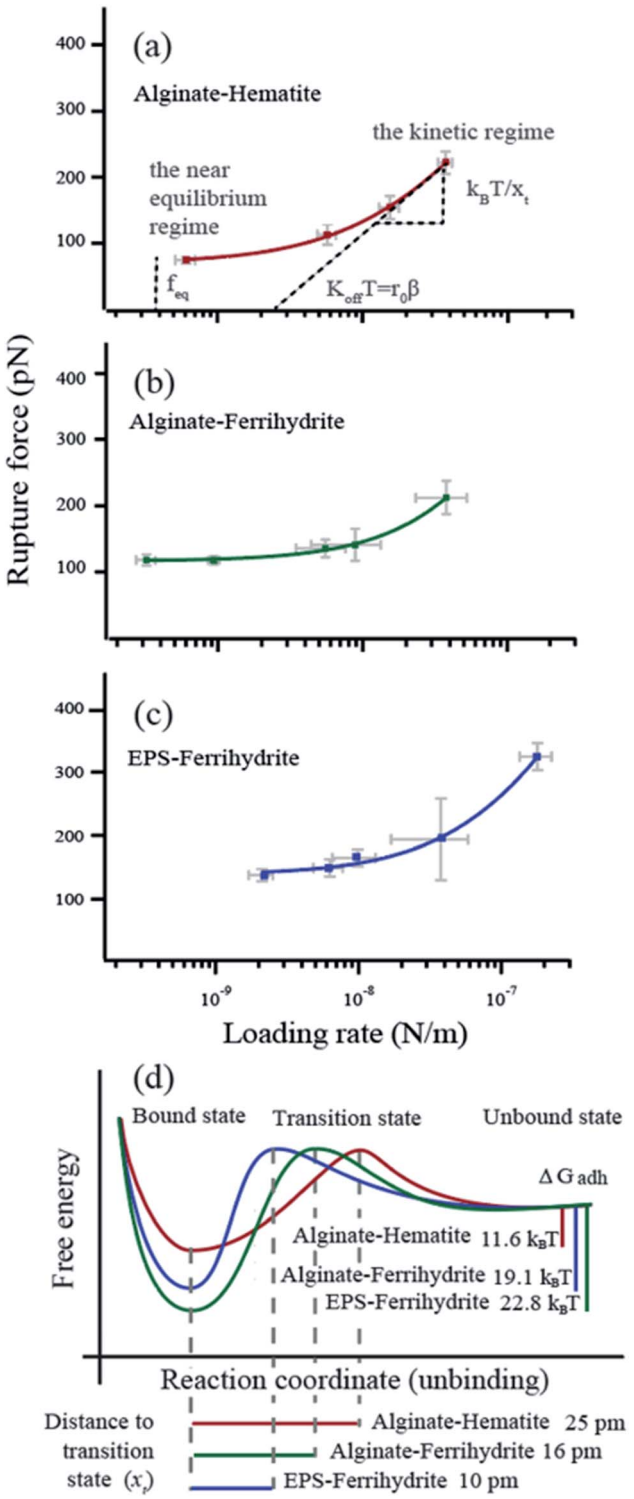

Fig. 2 Dynamic force data displayed as rupture force in pN *vs.* loading rate in N m^{-1} (a–c) The data points represent the values for each velocity pool with standard errors. The curve (red, purple or green) is a fit to the single bond model. The parameters obtained from the fitting are d listed in Table 1. The intercept between the plateau of rupture forces in the near equilibrium regime and the *y*-axis defines the f_{eq}, the slope of the kinetic regime defines the x_t and the intercept between a tangent of the kinetic regime and the *x*-axis (r_0) defines the k_{off} ($\beta = e^{-0.557}x_t/k_BT$). (d) Reaction coordinates for unbinding from a bound state. Alg-alginate; EPS-extracellular polymer substance; FHY-ferrihydrite; HEM-hematite; ΔG_{adh}-the crystal-polymer binding free energy.

Table 1 Bond parameters

	x_t[a] (pm)	k_{off}[b] (s^{-1})	f_{eq}[c] (pN)	ΔG_{adh}[d] (k_BT)
Alginate–hematite	25 ± 5	74 ± 18	71 ± 4	11.6 ± 0.6
Alginate–ferrihydrite	10 ± 8	240 ± 94	116 ± 2	19.1 ± 0.3
EPS–ferrihydrite	16 ± 8	307 ± 180	139 ± 6	22.8 ± 1.0

[a] x_t, the distance to the transition state. [b] k_{off}, the intrinsic unbinding rate. [c] f_{eq}, the equilibrium rupture force. [d] ΔG_{adh}, the crystal–polymer binding free energy. Numbers in grey represent the standard error.

arises from multiple rupture events. After extracting the curves approximating single polymer interactions[36] we plotted the average rupture force (f_r) for single polymers as a function of the average loading rate (l_r) of alginate–hematite, alginate–ferrihydrite and EPS–ferrihydrite systems (Fig. 2a–c). The observed trends for f_r *vs.* l_r exhibit the characteristic shape of DFS curves, that cross the two fundamental regimes of bond breaking: the near equilibrium plateau at low l_r and the kinetic regime of increasing f_r at high l_r[45,72] (grey text in Fig. 2a).

We applied the single bond analysis[45] adopted for polymers[36] to our dynamic force spectra (Fig. 2a–c) and extracted the equilibrium force (f_{eq}), the intrinsic unbinding rate (k_{off}), and the distance between transition states (x_t). Knowing f_{eq}, we obtained the crystal–polymer binding Gibbs free energy (ΔG_{adh}) using eqn (8)–(10). The parameters and standard errors are presented in Fig. 2d and Table 1. While the EPS–ferrihydrite bond properties are similar to those for alginate–ferrihydrite, both are distinct from the properties of the alginate–hematite bond. ΔG_{adh} is slightly higher for EPS–ferrihydrite (22.8 ± 1 k_BT) than for alginate–ferrihydrite (19.1 ± 0.3 k_BT) but both are nearly twice greater than for alginate–hematite (11.6 ± 0.6 k_BT). EPS–hematite was previously shown to be 8.6 k_BT (using a similar approach).[36] Similarly, x_t and k_{off} for the ferrihydrite systems are indistinguishable, within experimental error, whereas k_{off} is ~4 times smaller for the alginate–hematite bond. k_{off} is a measure of the kinetic barrier to bond breaking and the higher values for ferrihydrite imply that the bond strength of (E)PS to ferrihydrite is stronger than to hematite.

Effects of bond strength on iron oxide nucleation

The values of ΔG_{adh} can now be used to evaluate the impact of polymer–mineral interaction on γ and on ferrihydrite and hematite nucleation (eqn (2)). To calculate γ, we need the crystal–liquid interfacial free energy, γ_{CL}, which is difficult to measure experimentally but it is related to mineral solubility, C_{eq}, through an empirical approximation:[73]

$$\gamma_{CL} = -18.3 \log(C_{eq}) + 34.5. \quad (11)$$

particle size and solution speciation (Section 6 in ESI, Table S1†). Assuming hematite forms from aggregation of ferrihydrite,[28] we have used solubility data for 3 nm ferrihydrite and 6 nm hematite, which give γ_{CL} of 159 and 224 mJ m^{-2} (eqn (11), more details in Section 7-ESI†). Our γ_{CL} (ferrihydrite) = 159 mJ m^{-2} is comparable with the γ_{CL} (ferrihydrite) = 186 mJ m^{-2} estimate based on the thermodynamic data.[22] There are no

 This journal is © The Royal Society of Chemistry 2020

Open Access Article. Published on 15 June 2020. Downloaded on 4/30/2026 12:16:13 PM.
This article is licensed under a Creative Commons Attribution-NonCommercial 3.0 Unported Licence.

Table 2 Interfacial free energy, γ (mJ m^{-2}), as a function of h and a (nm2)[a]

	Alginate–hematite					Alginate–ferrihydrite					EPS–ferrihydrite				
ΔG_{adh}	28.8 kJ mol^{-1}					47.3 kJ mol^{-1}					56.5 kJ mol^{-1}				
γ_{CL}	224 mJ m^{-2}					159 mJ m^{-2}					159 mJ m^{-2}				
h/a	0.1	0.2	0.3	0.4	0.5	0.1	0.2	0.3	0.4	0.5	0.1	0.2	0.3	0.4	0.5
0.3	147	219	243	255	262	−30	88	128	148	159	−76	65	112	136	150
0.5	96	216	256	276	288	−156	41	107	140	160	−233	3	81	121	144
0.8	20	211	275	307	327	−345	−29	76	128	160	−457	−91	35	98	135

[a] γ for nucleation on the polymer as a function of area for possible interaction, a, and shape factor, h. Nucleation is favored (black) when $\gamma < \gamma_{CL}$ and unfavorable when $\gamma > \gamma_{CL}$ (grey). ΔG_{adh}, the crystal–polymer binding free energy.

estimates for γ_{CL} of nanoparticulate hematite but taking the value of 830 mJ m^{-2} estimated for bulk hematite[21,22] and knowing that its value ought to decrease with decreasing particle size, our estimate follows the trend. Using the values of ΔG_{adh} from the DFS measurements and γ_{CL} derived from the solubility, we derived γ for the realistic combinations of a and h (Table 2). The exact values of a and h for iron (oxyhydr)oxides nucleation in these systems are not known but based on polysaccharide configuration and possible nucleus shapes (*e.g.* h = 0.5 for a hemisphere)[32] we estimated possible ranges (Table S3, Section 8-ESI†). For ferrihydrite, both alginate and EPS decrease the interfacial free energy for nucleation compared with nucleation in the bulk solution (γ_{CL}) for most values of a and h (PS: $a \leq 0.4$ nm^2 and EPS: $a \leq 0.5$ nm^2). For alginate–hematite interactions, nucleation on the polymer is only favorable if a is extremely small, perhaps unreasonably so (Table 2). Adapting a smaller grain size for hematite gives slight favourable conditions for direct nucleation on the polymer if $a \leq 0.3$ nm^2, but is still below the ranges calculated for ferrihydrite.

The results raise the question of why EPS promotes iron oxide nucleation more than alginate. The bond dynamics explored here are expected to be driven by electrostatic interactions between negatively charged groups of EPS and alginate and positively charged iron oxide surface sites. First, we note that the covalent bond between polysaccharide molecules anchored to an AFM tip and the substrate breaks at about 2 nN (ref. 74) and our DFS data show that our measured rupture forces are well below such a value. Thus, the stronger f_{eq} and ΔG_{adh} found for EPS is likely to reflect compositional differences between EPS and alginate. In addition to COO^-, EPS also contains proteins and lipids.[42,75] The amine groups from the proteins are positively charged while the phosphate groups are negatively charged and both could contribute to binding. Beside the electrostatic contribution from the functional groups, the difference in f_{eq} between alginate–ferrihydrite and EPS–ferrihydrite could be caused by differences in steric effects between polymer and substrate and/or variations in oxygen–oxygen interactions between the functional groups.[32]

The solubilities for ferrihydrite and hematite are a function of in the DFS approach, we only measure the strongest bond, but in a bulk system, a number of bonds act between alginate and the mineral surface. We used DFT to compare the adsorption energy of the full alginate monomer and water molecules to a hematite {00.1} face. Even at neutral conditions, *i.e.*, where the interaction between the mineral surface and the alginate monomer exclude the electrostatic contribution, alginate adsorption still has a significantly more favorable adsorption

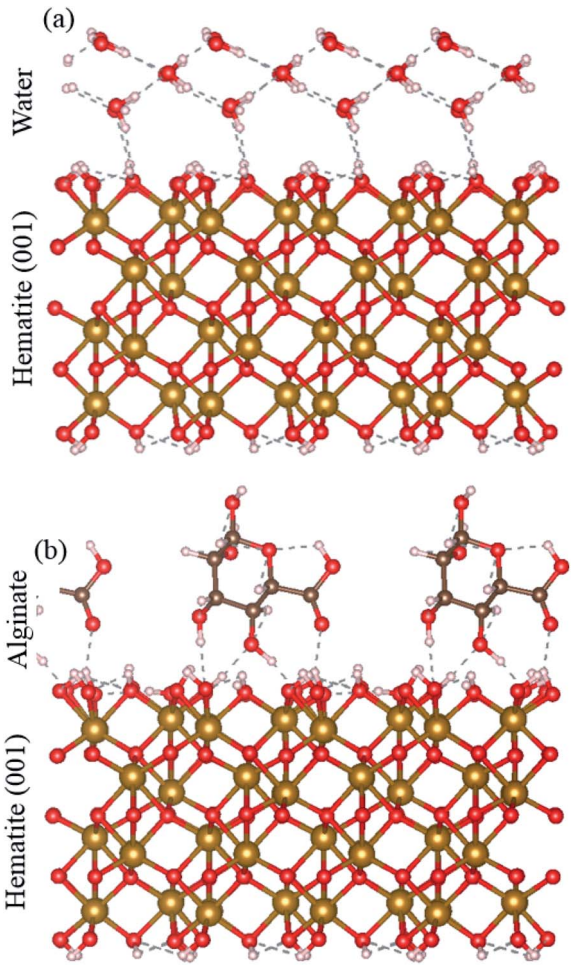

Fig. 3 DFT simulation of (a) hematite–water and (b) hematite–alginate binding.

Open Access Article. Published on 15 June 2020. Downloaded on 4/30/2026 12:16:13 PM.
This article is licensed under a Creative Commons Attribution-NonCommercial 3.0 Unported Licence.

energy than water (that represents a pure system). The alginate monomer binds to the hematite surface through two alcohol groups and a carboxyl group and involves a total of four hydrogen bonds; adsorption energy is −1.11 eV. In contrast, a single water molecule interacts with the surface through two hydrogen bonds; adsorption energy of −0.43 eV. Even under neutral conditions, the hematite–alginate bond is significantly more exothermic than the hematite–water bond (−1.11 *vs.* −0.43 eV per molecule) and the alginate interaction results in stronger surface binding per molecule than water (Fig. 3).

Nucleation in the bulk system: the size of ferrihydrite coprecipitated with alginate

The conclusion that polysaccharides, whether alginate or EPS, decrease the nucleation barrier for ferrihydrite formation is supported by a parallel set of experiments where ferrihydrite nanoparticles were coprecipitated with alginate (we did not attempt to coprecipitate hematite with alginate because alginate starts to degrade rapidly at water boiling temperature).

When the interfacial free energy is low, we expect more nucleation sites, promoting the growth of smaller crystals than in a system with fewer nucleation events. TEM (Fig. 4) and PDF analysis (details in Section 9-ESI†) of our precipitates show that the alginate-coprecipitated ferrihydrite particles are slightly smaller and that there is a high coverage of ferrihydrite particles on the polymer (essentially 100% in Fig. 4b). Although smaller crystals can also be produced if the growth of the nuclei is inhibited by the polymer, the qualitative TEM results are consistent with the conclusion that the biopolymers decrease the interfacial free energy which is expected to enhance nucleation rates of the iron (oxyhydr)oxides relative to nucleation in a solution.

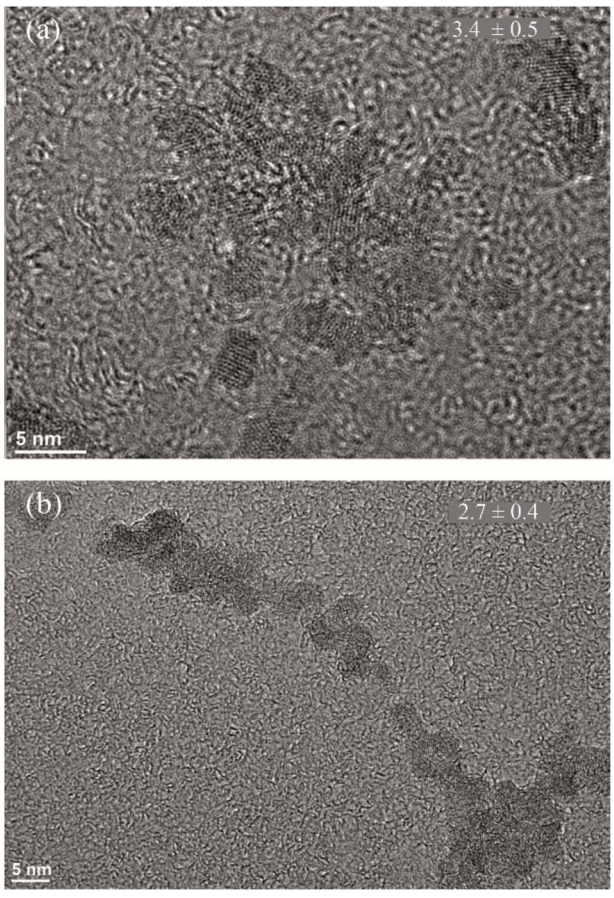

Fig. 4 TEM images of (a) pure ferrihydrite and (b) alginate–ferrihydrite. Average grain size in nm is given in the upper right corner for $n = 22$. Experiments done in duplicates.

The interfacial water of alginate–iron oxy(hydr)oxide complexes could play a role in their nucleation

The DFS results reported here imply that the polymer–mineral interaction alone could exert control over iron (oxyhydr)oxide nucleation. However, TGA and cryoXPS show that the role of the interactions between the polymer and the surrounding aqueous medium cannot be ignored. TGA indicates a higher water

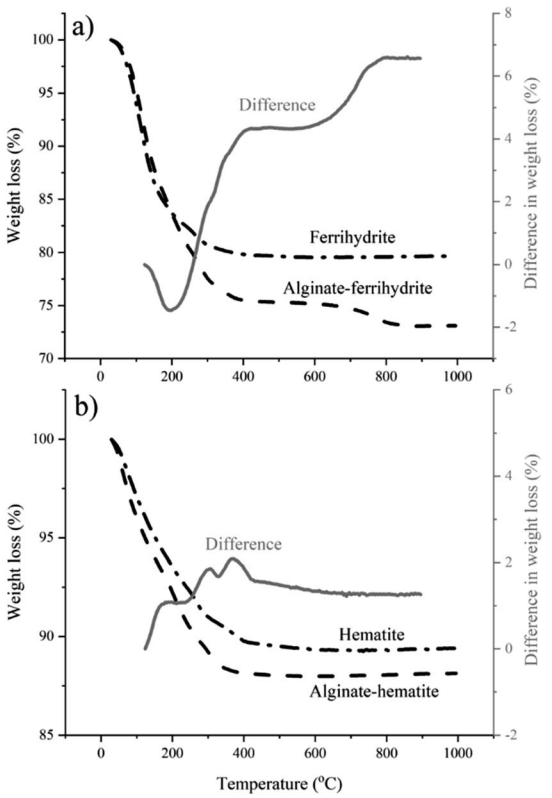

Fig. 5 TGA of ferrihydrite, hematite and their complexes with alginate. The gray curve represents the difference curve obtained by substraction of (a) TG curve of a pure ferrihydrite from the TG curve of ferrihydrite–alginate complex and (b) TG curve of a pure hematite from the TG curve of hematite–alginate complex. (a) The negative difference in weight loss between 100 and 200 °C indicates that alginate–ferrihydrite contains more water than pure ferrihydrite and that water is more tightly bound. The positive change in weight loss over the rest of the curve results from decomposition of the alginate in the alginate–ferrihydrite sample. (b) The difference in weight loss between 100 and 200 °C is positive suggesting no extra, tightly bound water in the alginate–hematite complex compared to pure hematite.

 This journal is © The Royal Society of Chemistry 2020

Open Access Article. Published on 15 June 2020. Downloaded on 4/30/2026 12:16:13 PM.
This article is licensed under a Creative Commons Attribution-NonCommercial 3.0 Unported Licence.

Table 3 Oxygen concentrations and calculated interfacial water content of alginate–ferrihydrite and alginate–hematite complexes

			O 1s[b] (atom %)	Interfacial H_2O content[c] (%)	ΔH_2O content (%)
Ferrihydrite	MilliQ	V[a]	90.1	8.4	+3.7
		RT[a]	81.7		
	0.1% alginate	V	68.6	12.1	
		RT	56.5		
Hematite	MilliQ	V	83.6	7.1	−1.8
		RT	76.5		
	0.1% alginate	V	70	5.3	
		RT	64.7		

[a] V-vitrified sample, *i.e.*, the spectrum from the sample analysed at cryogenic conditions, and RT-room temperature sample, *i.e.*, the spectrum acquired from the sample analysed at ambient temperature. [b] High-resolution spectra of O 1s region of all samples can be found in the ESI. [c] Values are calculated by subtracting the oxygen content of the RT sample from the V sample.

content in alginate–ferrihydrite complexes compared to pure ferrihydrite (Fig. 5a) and suggests a distinct difference in thermochemical properties between the two systems. This is not the case for alginate–hematite complex that shows similar thermochemical behavior to pure hematite (Fig. 5b).

These results were confirmed with cryoXPS measurements (more details in Section 10-ESI†). CryoXPS shows an increased interfacial water content of 3.7% in the alginate–ferrihydrite system compared to pure ferrihydrite (Table 3, Fig. S8†). In the alginate–hematite system, there is a decrease in the interfacial water content compared to pure hematite (Table 3, Fig. S9†). The reason for the decrease of the interfacial water content upon the complexation of hematite with alginate is unknown. This extra, more strongly bound water in the alginate–ferrihydrite interface region is expected to influence the interfacial energy and reaction rates and could explain increased ferrihydrite transformation rates in the central part of bacterial polysaccharide filaments.[3]

Conclusion

We investigated biopolymer induced precipitation of iron (oxyhydr)oxides by measuring the interfacial free energy of the polymer–nuclei-solution system. We looked into the precipitation of ferryhidrite and hematite because they are common iron biominerals. As model bacterial biopolymers, we used alginate polysaccharide and extracellular polymeric substance extracted from the biofilm of Shewanella oneidensis. We used dynamic force spectroscopy to determine the equilibrium force and Gibbs free energy of binding between ferrihydrite and hematite substrates and biopolymers. Our rationale was that the stronger the energy of binding, the lower the barrier towards nucleation. We used the Gibbs free energy of binding to determine the interfacial free energy of the biopolymer–iron (oxyhydr)oxide-solution system (heterogeneous nucleation) and compared it to the interfacial free energy of iron (oxyhydr)oxide-solution system (homogeneous nucleation).

The higher f_{eq} for ferrihydrite than hematite is likely caused by higher charge density at the surface. Microbial polymers can, through strong mineral binding (high f_{eq}), decrease the nucleation barriers for ferrihydrite and direct nucleation on the polymers. Our results for complex polymer systems parallel observations of the impact of organic molecules on carbonate mineral formation by marine organisms.[33,34] In both systems, the influence of the charge state of the polymer and polymer–solvent–mineral interactions, reflected in the polymer–mineral γ, suggests that electrostatic interactions are important for binding and in determining interfacial energies and hence, for controlling nucleation. In addition to electrostatic interactions, the DFT simulations suggest that hydrogen bonding might be an additional source of biopolymer–iron oxide binding. Our results on thermal stability and interfacial water content of polymer–mineral complexes imply that the polymer–solvent interactions can also impact the mineral transformation kinetics from the initial, transient disordered phase the final, stable phase. Thus, our data show that a combination of polymer–mineral and polymer–solvent interactions control the dynamics of iron oxide mineralization from the first appearance to final form. Finally, our results highlight that microbial polymers can decrease the barriers for nucleation which is expected to lead to enhanced nucleation of iron (oxyhydr)oxides at low driving forces.

Conflicts of interest

There are no conflicts to declare.

Acknowledgements

We sincerely thank Dr Halei Zhai, Dr Jinhui Tao and Dr Christina Newcomb for helpful discussion on DFS, Kirstine Bach for generation of 3D figures and renderings, Dr Nico Bovet for useful comments on cryoXPS, Dr Glen Waychunas for providing the hematite sample and Dr Caroline Ajo-Franklin and Dr Kevin Rosso for encouragement and intellectual input. Funding for data collection and interpretation and for molecular simulations was provided by the U.S. Department of Energy (DOE), Office of Basic Energy Sciences (OBES), Chemical Sciences, Geosciences and Biosciences Division through its Geosciences Program at Pacific Northwest National Laboratory (PNNL), which is operated by Battelle for the U.S. DOE under Contract DE-AC05-76RL01830. Analytical method development was

Open Access Article. Published on 15 June 2020. Downloaded on 4/30/2026 12:16:13 PM.
This article is licensed under a Creative Commons Attribution-NonCommercial 3.0 Unported Licence.

supported by Sandia National Laboratories, a multi-mission laboratory managed and operated by National Technology and Engineering Solutions of Sandia LLC, a wholly owned subsidiary of Honeywell International Inc. for the U.S. Department of Energy's National Nuclear Security Administration under contract DE-NA0003525. The research was performed using the Environmental and Molecular Sciences Laboratory, which is a DOE Office of Science Scientific User Facility (SUF) sponsored by the Office of Biological and Environmental Research operated by PNNL, under proposal 48274 and a U.S. DOE Office of Science Early Career Award (Project 60385). This research also used resources of U.S. DOE OBES SUFs, the Advanced Photon Source and the Molecular Foundry, which are operated for the DOE OBES by, respectively, Argonne National Laboratory under Contract No. DE-AC02-06CH11357 and LBNL under Contract No. DE-AC02-05CH11231. SJ, SD, KD and SLSS were supported by the running budget of the Materials Chemistry Research Section, University of Copenhagen.

Notes and references

1 K. O. Konhauser, *FEMS Microbiol. Rev.*, 1997, **20**, 315–326.
2 D. E. Canfield, *Nature*, 1998, **396**, 450.
3 C. S. Chan, G. D. Stasio, S. A. Welch, M. Girasole, B. H. Frazer, M. V. Nesterova, S. Fakra and J. F. Banfield, *Science*, 2004, **303**, 1656–1658.
4 J. Miot, K. Benzerara, G. Morin, A. Kappler, S. Bernard, M. Obst, C. Férard, F. Skouri-Panet, J.-M. Guigner, N. Posth, M. Galvez, G. E. Brown and F. Guyot, *Geochim. Cosmochim. Acta*, 2009, **73**, 696–711.
5 C. S. Chan, S. C. Fakra, D. C. Edwards, D. Emerson and J. F. Banfield, *Geochim. Cosmochim. Acta*, 2009, **73**, 3807–3818.
6 J. F. Banfield, S. A. Welch, H. Zhang, T. T. Ebert and R. L. Penn, *Science*, 2000, **289**, 751–754.
7 S. Vollrath, T. Behrends and P. V. Cappellen, *Geomicrobiol. J.*, 2012, **29**, 550–560.
8 S. Vollrath, T. Behrends, C. B. Koch and P. V. Cappellen, *Geochim. Cosmochim. Acta*, 2013, **108**, 107–124.
9 A. Zegeye, M. Etique, C. Carteret, C. Ruby, P. Schaaf and G. Francius, *J. Phys. Chem. C*, 2014, **118**, 5978–5987.
10 C. B. Kennedy, S. D. Scott and F. G. Ferris, *Chem. Geol.*, 2004, **212**, 269–277.
11 C. Mikutta, R. Mikutta, S. Bonneville, F. Wagner, A. Voegelin, I. Christl and R. Kretzschmar, *Geochim. Cosmochim. Acta*, 2008, **72**, 1111–1127.
12 C. W. Neil, J. R. Ray, B. Lee and Y.-S. Jun, *Environ. Sci.: Nano*, 2016, **3**, 647–656.
13 K. Eusterhues, A. Hädrich, J. Neidhardt, K. Küsel, T. F. Keller, K. D. Jandt and K. U. Totsche, *Biogeosciences*, 2014, **11**, 4953–4966.
14 R. E. Cooper, K. Eusterhues, C.-E. Wegner, K. U. Totsche and K. Küsel, *Biogeosciences*, 2017, **14**, 5171–5188.
15 U. Schwertmann and R. M. Cornell, in *The Iron Oxides*, John Wiley & Sons, Ltd, 2004, pp. 1–7.
16 J. Scheck, B. Wu, M. Drechsler, R. Rosenberg, A. E. S. Van Driessche, T. M. Stawski and D. Gebauer, *J. Phys. Chem. Lett.*, 2016, **7**, 3123–3130.
17 K. M. Towe and H. A. Lowenstam, *J. Ultra. Res.*, 1967, **17**, 1–13.
18 D. Li, M. H. Nielsen, J. R. I. Lee, C. Frandsen, J. F. Banfield and J. J. D. Yoreo, *Science*, 2012, **336**, 1014–1018.
19 J. Baumgartner, A. Dey, P. H. H. Bomans, C. Le Coadou, P. Fratzl, N. A. J. M. Sommerdijk and D. Faivre, *Nat. Mater.*, 2013, **12**, 310–314.
20 K. M. Ø. Jensen, H. L. Andersen, C. Tyrsted, E. D. Bøjesen, A.-C. Dippel, N. Lock, S. J. L. Billinge, B. B. Iversen and M. Christensen, *ACS Nano*, 2014, **8**, 10704–10714.
21 A. Navrotsky, L. Mazeina and J. Majzlan, *Science*, 2008, **319**, 1635–1638.
22 T. Hiemstra, *Geochim. Cosmochim. Acta*, 2015, **158**, 179–198.
23 U. Schwertmann and R. M. Cornell, in *Iron Oxides in the Laboratory*, John Wiley & Sons, Ltd, Weinheim, Federal Republic of Germany, 2nd edn, 2000, pp. 121–134.
24 G. Waychunas, T. Trainor, P. Eng, J. Catalano, G. Brown, J. Davis, J. Rogers and J. Bargar, *Anal. Bioanal. Chem.*, 2006, **386**, 2255.
25 T. Hiemstra and W. H. Van Riemsdijk, *Geochim. Cosmochim. Acta*, 2009, **73**, 4423–4436.
26 C. M. Flynn, *Chem. Rev.*, 1984, **84**, 31–41.
27 M. Zhu, C. Frandsen, A. F. Wallace, B. Legg, S. Khalid, H. Zhang, S. Mørup, J. F. Banfield and G. A. Waychunas, *Geochim. Cosmochim. Acta*, 2016, **172**, 247–264.
28 U. Schwertmann and E. Murad, *Clays Clay Miner.*, 1983, **31**, 277–284.
29 Y. Cudennec and A. Lecerf, *J. Solid State Chem.*, 2006, **179**, 716–722.
30 P. J. M. Smeets, K. R. Cho, R. G. E. Kempen, N. A. J. M. Sommerdijk and J. J. De Yoreo, *Nat. Mater.*, 2015, **14**, 394–399.
31 A. E. Nielsen, *J. Cryst. Growth*, 1984, **67**, 289–310.
32 Q. Hu, M. H. Nielsen, C. L. Freeman, L. M. Hamm, J. Tao, J. R. I. Lee, T. Y. J. Han, U. Becker, J. H. Harding, P. M. Dove and J. J. D. Yoreo, *Faraday Discuss.*, 2013, **159**, 509–523.
33 A. J. Giuffre, L. M. Hamm, N. Han, J. J. D. Yoreo and P. M. Dove, *Proc. Natl. Acad. Sci. U.S.A.*, 2013, **110**, 9261–9266.
34 L. M. Hamm, A. J. Giuffre, N. Han, J. Tao, D. Wang, J. J. D. Yoreo and P. M. Dove, *Proc. Natl. Acad. Sci. U.S.A.*, 2014, **111**, 1304–1309.
35 J. J. D. Yoreo and P. G. Vekilov, *Rev. Mineral. Geochem.*, 2003, **54**, 57–93.
36 K. K. Sand, R. W. Friddle and J. J. DeYoreo, *Sci. Rep.*, 2017, **7**, 8663.
37 J. Wingender, T. R. Neu and H.-C. Flemming, in *Microbial Extracellular Polymeric Substances: Characterization, Structure and Function*, ed. J. Wingender, T. R. Neu and H.-C. Flemming, Springer Berlin Heidelberg, Berlin, Heidelberg, 1999, pp. 1–19.
38 C. S. Hassler, V. Schoemann, C. M. Nichols, E. C. V. Butler and P. W. Boyd, *Proc. Natl. Acad. Sci. U.S.A.*, 2011, **108**, 1076.
39 C. S. Hassler, E. Alasonati, C. A. Mancuso Nichols and V. I. Slaveykova, *Mar. Chem.*, 2011, **123**, 88–98.

 This journal is © The Royal Society of Chemistry 2020

Open Access Article. Published on 15 June 2020. Downloaded on 4/30/2026 12:16:13 PM.
This article is licensed under a Creative Commons Attribution-NonCommercial 3.0 Unported Licence.

40 S. Jelavić, D. J. Tobler, T. Hassenkam, J. J. D. Yoreo, S. L. S. Stipp and K. K. Sand, *Chem. Commun.*, 2017, **53**, 12700–12703.
41 Y.-S. Jun, B. Lee and G. A. Waychunas, *Environ. Sci. Technol.*, 2010, **44**, 8182–8189.
42 B. Cao, L. Shi, R. N. Brown, Y. Xiong, J. K. Fredrickson, M. F. Romine, M. J. Marshall, M. S. Lipton and H. Beyenal, *Environ. Microbiol.*, 2011, **13**, 1018–1031.
43 M. Sletmoen and B. T. Stokke, *Biomacromolecules*, 2004, **5**, 1288–1295.
44 N. A. Burnham, X. Chen, C. S. Hodges, G. A. Matei, E. J. Thoreson, C. J. Roberts, M. C. Davies and S. J. B. Tendler, *Nanotechnology*, 2002, **14**, 1–6.
45 R. W. Friddle, A. Noy and J. J. D. Yoreo, *Proc. Natl. Acad. Sci. U.S.A.*, 2012, **109**, 13573–13578.
46 A. Noy and R. W. Friddle, *Methods*, 2013, **60**, 142–150.
47 S. Manohar and A. Jagota, *Phys. Rev. E: Stat., Nonlinear, Soft Matter Phys.*, 2010, **81**, 021805.
48 S. Manohar, A. R. Mantz, K. E. Bancroft, C.-Y. Hui, A. Jagota and D. V. Vezenov, *Nano Lett.*, 2008, **8**, 4365–4372.
49 M. A. K. Williams, A. Marshall, R. G. Haverkamp and K. I. Draget, *Food Hydrocolloids*, 2008, **22**, 18–23.
50 P. E. Blöchl, *Phys. Rev. B: Condens. Matter Mater. Phys.*, 1994, **50**, 17953–17979.
51 G. Kresse and D. Joubert, *Phys. Rev. B: Condens. Matter Mater. Phys.*, 1999, **59**, 1758–1775.
52 G. Kresse and J. Hafner, *Phys. Rev. B: Condens. Matter Mater. Phys.*, 1993, **47**, 558–561.
53 G. Kresse and J. Furthmüller, *Phys. Rev. B: Condens. Matter Mater. Phys.*, 1996, **54**, 11169–11186.
54 G. Kresse and J. Furthmüller, *Comput. Mater. Sci.*, 1996, **6**, 15–50.
55 J. P. Perdew, K. Burke and M. Ernzerhof, *Phys. Rev. Lett.*, 1996, **77**, 3865–3868.
56 J. P. Perdew, K. Burke and M. Ernzerhof, *Phys. Rev. Lett.*, 1997, **78**, 1396.
57 S. L. Dudarev, G. A. Botton, S. Y. Savrasov, C. J. Humphreys and A. P. Sutton, *Phys. Rev. B: Condens. Matter Mater. Phys.*, 1998, **57**, 1505–1509.
58 X. Huang, S. K. Ramadugu and S. E. Mason, *J. Phys. Chem. C*, 2016, **120**, 4919–4930.
59 R. L. Blake, R. E. Hessevick, T. Zoltai and L. W. Finger, *Am. Mineral.*, 1966, **51**, 123–129.
60 L. E. Barton, K. E. Grant, T. Kosel, A. N. Quicksall and P. A. Maurice, *Environ. Sci. Technol.*, 2011, **45**, 3231–3237.
61 A. P. Hammersley, S. O. Svensson and A. Thompson, *Nucl. Instrum. Methods Phys. Res., Sect. A*, 1994, **346**, 312–321.
62 P. J. Chupas, X. Qiu, J. C. Hanson, P. L. Lee, C. P. Grey and S. J. L. Billinge, *J. Appl. Crystallogr.*, 2003, **36**, 1342–1347.
63 X. Qiu, J. W. Thompson and S. J. L. Billinge, *J. Appl. Crystallogr.*, 2004, **37**, 678.
64 F. M. Michel, V. Barrón, J. Torrent, M. P. Morales, C. J. Serna, J.-F. Boily, Q. Liu, A. Ambrosini, A. C. Cismasu and G. E. Brown, *Proc. Natl. Acad. Sci. U.S.A.*, 2010, **107**, 2787–2792.
65 C. L. Farrow, P. Juhas, J. W. Liu, D. Bryndin, E. S. Božin, J. Bloch, T. Proffen and S. J. L. Billinge, *J. Phys.: Condens. Matter*, 2007, **19**, 335219.
66 F. M. Michel, L. Ehm, S. M. Antao, P. L. Lee, P. J. Chupas, G. Liu, D. R. Strongin, M. A. A. Schoonen, B. L. Phillips and J. B. Parise, *Science*, 2007, **316**, 1726–1729.
67 A. Shchukarev and S. Sjöberg, *Surf. Sci.*, 2005, **584**, 106–112.
68 A. Shchukarev, *Adv. Colloid Interface Sci.*, 2006, **122**, 149–157.
69 A. Shchukarev and M. Ramstedt, *Surf. Interface Anal.*, 2017, **49**, 349–356.
70 K. Shimizu, A. Shchukarev, P. A. Kozin and J.-F. Boily, *Langmuir*, 2013, **29**, 2623–2630.
71 S. Jelavić, A. R. Nielsen, S. L. S. Stipp and N. Bovet, *Langmuir*, 2018, **34**, 7011–7020.
72 R. W. Friddle, P. Podsiadlo, A. B. Artyukhin and A. Noy, *J. Phys. Chem. C*, 2008, **112**, 4986–4990.
73 O. Söhnel, *J. Cryst. Growth*, 1983, **63**, 174–176.
74 M. Grandbois, M. Beyer, M. Rief, H. Clausen-Schaumann and H. E. Gaub, *Science*, 1999, **283**, 1727–1730.
75 B. Cao, B. Ahmed, D. W. Kennedy, Z. Wang, L. Shi, M. J. Marshall, J. K. Fredrickson, N. G. Isern, P. D. Majors and H. Beyenal, *Environ. Sci. Technol.*, 2011, **45**, 5483–5490.